Nano-Micro Letters
e-ISSN 2150-5551
CN 31-2103/TB
ARTICLE
https://doi.org/10.1007/s40820-026-02090-2

Cite as
Nano-Micro Lett.
(2026) 18:239

Received: 3 October 2025
Accepted: 10 January 2026

Optical Switching of Robust Ferroelectric Polarization on Epitaxial $Hf_{0.5}Zr_{0.5}O_2$ Integrated with $BaTiO_3$

Wenjing Dong[1], Huan Tan[2], Jingye Zou[1], Alberto Quintana[1], Tingfeng Song[1], César Magén[3,4], Claudio Cazorla[5,6,7], Florencio Sánchez[1] ✉, Ignasi Fina[1] ✉

HIGHLIGHTS

- Integration of perovskite $BaTiO_3$ with epitaxial fluorite $Hf_{0.5}Zr_{0.5}O_2$ is demonstrated.
- Polarization up to 15 μC cm^{-2}, leakage current densities below 10^{-6} A cm^{-2}, endurance up to 10^8 cycles, and switching times shorter than 50 ns are achieved.
- Remote optical switching of the polarization is demonstrated, and it is shown to be controlled by the thickness of the $BaTiO_3$ capping layer.

ABSTRACT Optical switching of ferroelectric polarization is of interest for wireless and energy-efficient control of logic states. So far, this phenomenon has been widely demonstrated only in ferroelectric perovskites, while studies on other emerging ferroelectrics remain limited. In this regard, the paradigmatic example of a technologically relevant ferroelectric material is HfO_2. However, HfO_2 has a very wide bandgap, limiting light absorption. So far, the proposed strategies to enhance light absorption in HfO_2-based systems are detrimental to ferroelectric properties, i.e., bandgap lowering or on-purpose defect introduction, which reduce switchable polarization and increase the presence of leakage currents. Here, we show that good ferroelectric properties, i.e., sizeable polarization (up to 15 μC cm^{-2}), low leakage current (under 10^{-6} A cm^{-2}), high endurance (up to 10^8 cycles) and fast switching (< 50 ns), can be achieved in epitaxial $Hf_{0.5}Zr_{0.5}O_2$ films through an alternative strategy, $BaTiO_3$ capping. While ferroelectric properties are remarkable, we demonstrate that the presence of $BaTiO_3$ allows light absorption and the concomitant electric field generation, as supported by density functional theory calculations, which enables optical switching of polarization in $Hf_{0.5}Zr_{0.5}O_2$ under 405 nm illumination. It is observed that optical switching is more efficient in films with thicker $BaTiO_3$ capping layer. The high polarizability of $BaTiO_3$ contributes to minimizing degradation in the ferroelectric response of the system. The results presented here indicate that appropriate designs can be followed to obtain optical switching of polarization in ferroelectric HfO_2 while preserving main functional properties.

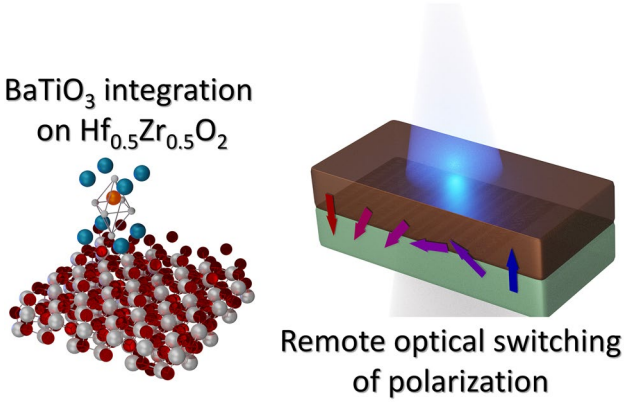

KEYWORDS HfO_2; Hafnium oxide; Multilayers; $Hf_{0.5}Zr_{0.5}O_2$; Ferroelectric; Optoelectric

✉ Florencio Sánchez, fsanchez@icmab.es; Ignasi Fina, ifina@icmab.es
[1] Institut de Ciència de Materials de Barcelona (ICMAB-CSIC), Campus UAB, 08193 Bellaterra, Barcelona, Spain
[2] Departament de Física, Universitat Autònoma de Barcelona, 08193 Cerdanyola del Vallès, Spain
[3] Instituto de Nanociencia y Materiales de Aragón (INMA), CSIC-Universidad de Zaragoza, 50009 Saragossa, Spain
[4] Departamento de Física de la Materia Condensada, Universidad de Zaragoza, 50018 Saragossa, Spain
[5] Group of Characterization of Materials, Departament de Física, Universitat Politècnica de Catalunya, Campus Diagonal Besòs, Av. Eduard Maristany 10–14, 08019 Barcelona, Spain
[6] Research Center in Multiscale Science and Engineering, Universitat Politècnica de Catalunya, Campus Diagonal-Besòs, Av. Eduard Maristany 10–14, 08019 Barcelona, Spain
[7] Institució Catalana de Recerca I Estudis Avançats (ICREA), Passeig Lluís Companys 23, 08010 Barcelona, Spain

Published online: 06 February 2026

1 Introduction

Ferroelectric memories have been on the market for more than 30 years. These are competitive in terms of power consumption, speed, retention, and endurance. However, these are based on $Pb(Zr,Ti)O_3$ (PZT) [1], which has the drawbacks of toxicity and low memory density. The reason for the low memory density capability is that PZT does not allow 3D integration processes and the node size in memory devices based on it cannot be scaled down below ~ 130 nm [2, 3]. Among all the ferroelectric materials, the scientific community has recently focused its attention on ferroelectric hafnium oxide [4]. The reason is that it is the most robust ferroelectric material fully compatible with complementary metal oxide semiconductor (CMOS) technology, and thus improved memory density can be achieved. Remarkably, ferroelectric memory devices at commercialization stage have been already reported [5, 6]. So far, research on hafnium oxide has primarily concentrated on polycrystalline films [2, 3].

Memory devices based on ferroelectric materials aim to involve only electronic processes [7], which are intrinsically energy-efficient [8]. The combination of ferroelectric materials with magnetic materials [9] or the use of the inherent large photovoltaic response of ferroelectrics [10] has been reported to result in further reduction of energy consumption for both the writing and reading processes. Exclusive phenomena related to the presence of ferroelectric polarization and its interaction with light are large photostrictive coefficients [11] and large open-circuit voltages [12]. Photostriction in ferroelectric/magnetic heterostructures has been used to modify magnetic properties with light [13–15]. Additionally, optoelectronic devices leveraging the presence of internal electric fields generated by ferroelectric polarization [16, 17] and memory cells based on light-controlled-polarization-dependent photoconductance [10, 18] have been developed. Recently, it has been shown that the population of polar domains with different orientations and associated domain walls in ferroelectric multidomain $BaTiO_3$ (BTO) single crystals, can be modulated by suitable coherent illumination [19, 20] or ultrafast light pulses [21], giving an additional path for investigation. The use of subsidiary devices [22, 23] has been reported to allow reversible optical switching of polarization. Light absorbed at semiconducting electrodes (e.g., MoS_2) can also trigger polarization switching as demonstrated in three-terminal ferroelectric field-effect transistor [24, 25]. In two-terminal ultrathin BTO junctions, light has been demonstrated to modify the tunneling [26, 27] or Schottky-limited [28] current as a consequence of polarization switching. Therefore, optical switching of polarization is a feasible and extremely interesting strategy from an applications perspective. Unfortunately, none of the ferroelectric materials in which optical switching has been investigated in the past is CMOS-compatible. This calls for studies on optical switching in HfO_2-based devices.

Regarding optical control of ferroelectric polarization in hafnium oxide, it must be noted that its bandgap is wide [≈ 6.0 eV for $Hf_{0.5}Zr_{0.5}O_2$ (HZO)] [29, 30], making it transparent to visible light (Fig. 1a) and therefore very few reports can be found on the effect of light in this material. Electrode, interfaces and/or defects [31–34] have been reported to allow light absorption. Similar is the case for ZrO_2 [35]. Regardless of the strategy employed to enable photoabsorption, optical polarization switching in hafnia has been reported to be possible by light-induced internal electric fields [32]. However, in the reported devices polarization is near 2 μC cm^{-2}, well below the polarization values required for applications (see Table 1). This is a consequence of the defective nature of the studied systems, which show visible light absorption at the expense of poorer ferroelectric properties. In addition, no reports on device endurance under illumination are available, which is a crucial technological parameter.

Therefore, it is necessary to study the combination of absorbing materials with ferroelectric hafnia and to mitigate the detrimental impact on technological parameters. With this aim, we have combined epitaxial ferroelectric $Hf_{0.5}Zr_{0.5}O_2$ (HZO) with a light absorbing material. In 2018, it was reported the epitaxial growth of ferroelectric hafnia on perovskite $SrTiO_3$(001) (STO) substrates using pulsed laser deposition (PLD) [36, 37], with good retention and endurance and without the presence of prominent wake-up effects [38]. Epitaxial films, although not CMOS compatible, are of the highest interest for the understanding of the intrinsic properties of the material [39]. Despite the large lattice mismatch between HfO_2 and $La_{0.67}Sr_{0.33}MnO_3$ (LSMO), ferroelectric HfO_2 grows with excellent properties on LSMO by the unconventional domain matching epitaxy mechanism [40]; however, this is not possible with other perovskite such

https://doi.org/10.1007/s40820-026-02090-2

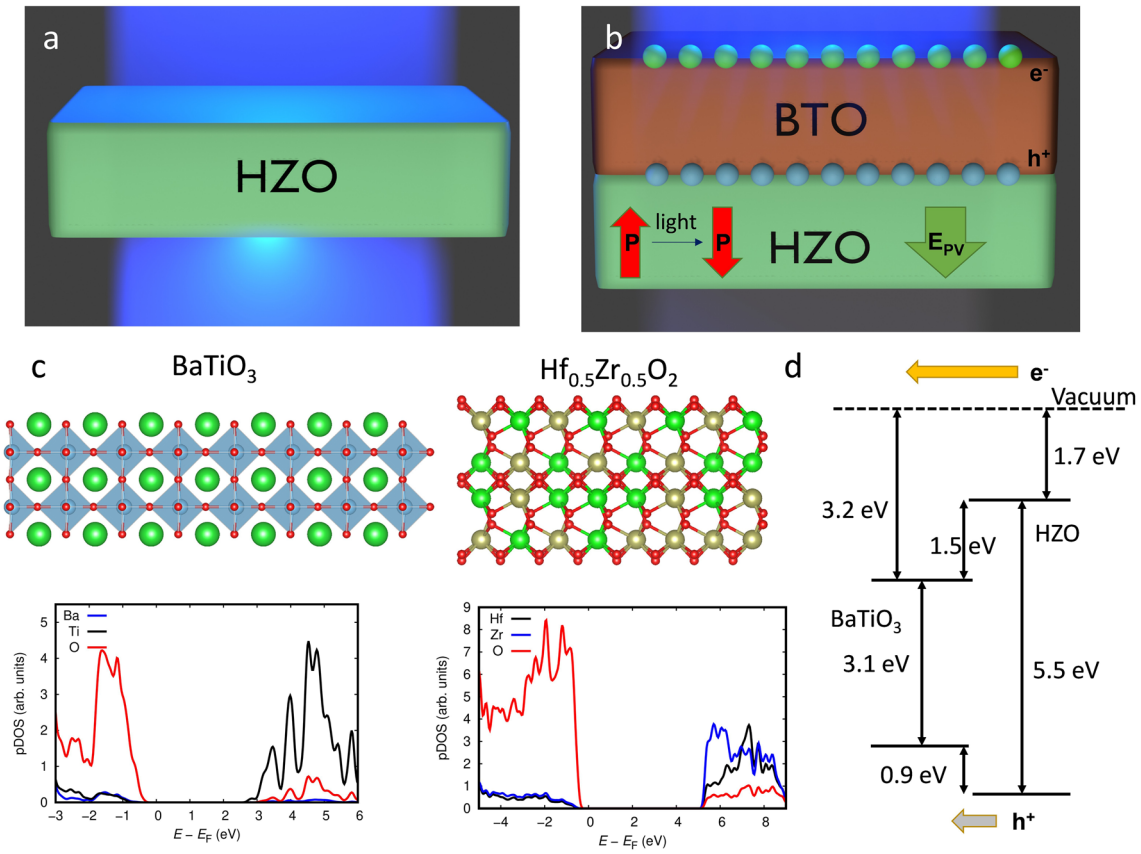

Fig. 1 Schematic representation of **a** the transparency of the HZO layer under illumination with 3.06 eV light and **b** the partial absorption of light, generation of E_{PV} and switching of ferroelectric polarization in presence of the top BTO layer. **c** Sketch of the structures for BTO and HZO used in DFT calculations and obtained density of states. **d** Computed band diagram for the BTO/HZO junction from first-principles DFT calculations

as $LaNiO_3$ or $SrRuO_3$ [41]. Interest in perovskite materials within the scientific community has intensified during the last years [42–44]. Here, we demonstrate that BTO can be integrated on top of epitaxial HZO while preserving good crystalline quality for both layers and the system ferroelectric response, concomitantly with visible-light absorption enhancement. BTO has been chosen due to its lower coercive field (E_c) compared to ferroelectric hafnium oxide. This makes BTO highly polarizable and therefore the presence of large depolarization fields is mitigated. At the same time the presence of photovoltaic effects in BTO using light in or near to the visible range is well-known [45–47]. In a HZO/BTO bilayer structure (Fig. 1b), light absorption at BTO and the concomitant presence of photovoltaic effect guarantees the generation of charges. These charges accumulate generating the presence of an additional electric field (E_{PV}, directed downwards in the figure for convenience). The direction of this E_{PV} will dictate the final polarization direction from up to down in the Fig. 1b. Indeed, we performed first-principles calculations based on density functional theory (DFT) to obtain the band gaps of the BTO and HZO slabs depicted in Fig. 1c. To estimate band alignments, we performed DFT calculations in combination with the range-separated hybrid functional HSE06 [48], a computational approach described in previous works [49, 50], to obtain electronic configuration of BTO and HZO layers. In Fig. 1c, the density of states of both materials is also included. For BTO, the valence band (VB) is clearly dominated by O-*p*–type orbitals, which hybridize with Ti-*d* and Ba-*p*,*d* orbitals. On the other hand, the conduction band (CB) is dominated by Ti-*d*–type orbitals, which mainly hybridize with O-*p* orbitals. For HZO, the VB is also clearly dominated by O-*p*–type orbitals that hybridize with Hf-d orbitals. In addition, Zr-*d* orbitals participate together with Hf-d orbitals in the VB and dominate in the CB. In Fig. 1d, the resulting band alignment is depicted. It can be observed the presence of a straddling gap at the HZO/

Table 1 Summary of remanent polarization (P_r) values in different systems based on HfO_2 or ZrO_2 where optoelectric response has been characterized. It is also indicated if the optical switching of polarization has been observed and if endurance tests have been performed

System	P_r (μC cm^{-2})	Reliability test	Wavelength (nm)	Optical switching time	Refs.
Si//HfO_2/AgNWs	2.5–4.96	no	940	NE	[31]
Nb:$SrTiO_3$//HZO/Pt	1	no	405–648	1 s	[32]
Si//HfO_2/Al:HfO_2/Al_2O_3/Graphene/Au	1.92	no	532	Apparent*	[33]
Si//Si:HfO_2/TiN	not given	no	AM1.5	NE	[34]
ITO//ZrO_2/SiOx/Si/Al	1.2	no	940	NE	[35]
$SrTiO_3$//LSMO/HZO/BTO/Pt	15	yes	405	~ 1 s	Present work

*Apparent accounts for the observation of memory effects without direct demonstration of the optical switching. NE: not evaluated. AM1.5 denotes the standard terrestrial solar spectrum corresponding to an air mass of 1.5

BTO interface. Under illumination, electron–hole pairs are generated in the heterostructure. Under open-circuit conditions, photogenerated carriers cannot flow through the external circuit; as a result, electrons are driven toward and accumulate at the BTO top surface. Correspondingly, holes accumulate at the BTO/HZO interface, since the HZO layer remains insulating under illumination due to its optical transparency. This charge separation gives rise to a net downward E_{PV}, as illustrated in Fig. 1b, which in turn drives the downward optical switching of polarization. It is important to emphasize that it has been reported that BTO ferroelectric order can vanish by the application of light [26, 27, 51, 52].

To test the proposed scenario for achieving optical switching of the polarization in structures based on ferroelectric HfO_2, here we investigated a series of BTO capped HZO samples variable BTO layer thickness. The HZO/BTO bilayers were deposited on LSMO electrodes on STO substrates by PLD. We show that BTO grows in polycrystalline form on top of the epitaxial HZO. Endurance properties are reported to be robust and switching time fast with and without illumination. Optical switching of polarization occurs in samples where the BTO layer is thick enough to allow abundant generation of photogenerated charges to produce polarization switching.

2 Experimental

2.1 Sample Fabrication

Five HZO/BTO bilayers, with HZO thickness 8 nm and BTO layer thickness ranging from 1.5 to 100 nm, were grown by PLD on top of the LSMO electrodes deposited on STO(001) substrates. Two HZO/BTO bilayers, with HZO thickness 2 and 4 nm and BTO layer thickness of 10 nm, were also grown for comparison. An additional bare HZO film of 8 nm and a single BTO film of 100 nm were grown to be used as references. The (001)-oriented LSMO bottom layer, with a thickness of 25 nm, was deposited under dynamic oxygen pressure (PO_2) of 0.1 mbar and at a substrate temperature (T_s) of 700 °C. Subsequently, the HZO layer was deposited under the same PO_2 of 0.1 mbar but at T_s of 800 °C. BTO layers were finally deposited on top, with PO_2 of 0.02 mbar and at T_s of 700 °C. Platinum top electrodes, 20 nm thick and 20 μm in diameter, were deposited onto the samples using dc magnetron sputtering through a stencil mask and these are shown in top planar view in Supporting Informations.

2.2 X-Ray Characterization

The crystal structure was analyzed using X-ray diffraction (XRD) with Cu Kα radiation on a Bruker D8 Discover diffractometer equipped with a point detector. A Bruker D8-Advance diffractometer, equipped with a two-dimensional detector was also used.

2.3 Scanning Transmission Electron Microscopy

Atomic-scale structural analysis of selected films was performed by scanning transmission electron microscopy (STEM) in high-angle annular dark field (HAADF) imaging mode. A Thermo Fisher Titan 60–300 microscope equipped with a high brightness Schottky field emission gun and a CETCOR probe-corrector (CEOS Gmbh) was operated at 300 kV to provide a probe size below 0.1 nm.

https://doi.org/10.1007/s40820-026-02090-2

Cross-sectional lamellae of the specimens, cut along (110) planes of the STO substrate, were prepared by focused ion beam milling in a Thermo Fisher Helios 650 Nanolab.

2.4 Ferroelectric Characterization

Ferroelectric polarization and current versus voltage loops and endurance were measured at room temperature using an AixACCT TFAnalyser3000 platform in a top–bottom configuration [53], with the bottom electrode grounded and the top electrode biased. To compensate leakage in polarization loops, the dynamic leakage current compensation (DLCC) and positive-up-negative-down (PUND) methods were employed [54, 55]. Endurance tests were carried out using 1 MHz bipolar electric field pulses, with remanent polarization determined positive and negative polarization values from DLCC loops measured at 1 kHz at the same electric field. The pulse train used for switching dynamics experiments is described as follows. Firstly, a preswitching pulse is applied. This is long enough to ensure the polarization saturation at indicated in the manuscript electric field. Afterwards, a trapezoidal switching of rise/fall/plateau time (τ_w) pulse is applied. After 1 s, a modified PUND pulse train is used for polarization state reading (ΔP) [56]. The leakage current was measured using 2 s integration time, with data averaged during both increasing and decreasing voltage sweeps. In the experiments performed under illumination, the device under test is continuously illuminated by light.

2.5 Piezoelectric Force Microscopy Characterization

Piezoelectric force microscopy (PFM) measurements were taken with an MFP-3D microscope (Oxford Instruments Co.) using BudgetSensors silicon (n-type) cantilevers with Pt coating (Multi75E-G). To enhance sensitivity, the dual AC resonance tracking (DART) method was employed [64]. To remove charging effects contribution additional bias voltage was also employed during PFM characterization [65].

2.6 Optical Excitation

Optical illumination during or after electrical tests or PFM tests was performed with a blue-violet laser source ($\lambda = 405$ nm, $E_{photon} = 3.06$ eV, power density ≈ 3.9 W cm^{-2}). Note that at this wavelength the 20 nm thick Pt top electrode transparency is around 15% [57]. The incidence angle was fixed for all the measurements at $\approx 45°$. Note that the energy of the used light (blue-violet; 3.06 eV) is below the bandgap energy of BTO (whose bandgap in bulk is about 3.3 eV [58]), and then band-to-band excitation cannot be produced. However, in BTO films, it is known that significant photon absorption can occur for sub-bandgap photon energies [59–61]. This is a result of the presence of oxygen vacancies or other point defects in BTO introducing allowed states within the bandgap [59, 62, 63].

2.7 First-Principles Calculations

First-principles calculations based on DFT [66]. were carried out with the PBEsol exchange–correlation energy functional [67] as it is implemented in the VASP software [68]. The "projector-augmented wave" method [69] was employed to represent the ionic cores by considering the following electronic states as valence: Hf 5*d* 6*s* 5*p*; Zr 4*d* 5*s* 4*p*; O 2*s* 2*p*; Ba 5*s* 5*p* 6*s*; Ti 3*d* 4*s* 3*p*. An energy cutoff of 650 eV and a dense Monkhorst–Pack k-point density (equivalent to that of a $12 \times 12 \times 12$ grid for the 12-atom bulk HfO_2 unit cell) was used for integration within the Brillouin zone, leading to total energies converged to within 1 meV per formula unit. Atomic relaxations were concluded when the forces in all the atoms were below 0.005 eV Å^{-1}. The simulated HZO slab contained a total of 48 atoms (16 Hf and 32 O ions), extending over a length of approximately 40 Å perpendicular to its surface (with a 20 Å thick vacuum region). Similarly, the simulated BTO slab contained a total of 160 atoms (32 Ba, 32 Ti and 96 O ions), extending over a length of approximately 50 Å perpendicular to its surface (with a 25 Å thick vacuum region). The materials band gaps were calculated using the range-separated hybrid functional HSE06 [48]. To estimate band alignments, we followed the computational approach described elsewhere [49, 50].

3 Results

3.1 $Hf_{0.5}Zr_{0.5}O_2/BaTiO_3$ Heterostructure Integration

Representative HZO/BTO bilayers with 0, 1.5, 10, and 100 nm for the BTO are sketched in Fig. 2a-d, respectively. Platinum circular top electrodes were deposited onto the whole set of samples with 0, 1.5, 5, 10, 30, and 100 nm for the BTO layer, and these are shown in Fig. S1. HZO thicknesses are ≈ 8 nm for all films as extracted from the simulation of the Laue fringes in the θ-2θ XRD scans (Fig. S2). The BTO thicknesses were calculated from calibration of the growth rate. XRD 2θ-χ maps for the single-layer and the HZO/BTO representative samples of thickness 0, 1.5, 10, and 100 nm for the BTO layer are shown in Fig. 2e-h, respectively. The spots of highest intensity correspond to STO(001) and STO(002). The presence of the spot at 2θ ≈ 30° indicates the formation of the orthorhombic phase with (111) orientation. Monoclinic (m) (002) elongated spot ($2\theta \approx 35°$) is present in the sample capped with 1.5 nm BTO (Fig. 2f). The elongation of the spot along χ indicates a higher mosaicity of monoclinic crystals compared with the orthorhombic ones. The intensity of this diffraction spot is lower in the other samples. In the sample capped with 100 nm BTO (Fig. 2h), the arc corresponding to BTO(101) ($2\theta \approx 31°$) crystallites indicates its polycrystalline growth. Integrated around $\chi \approx 0°$, 2θ scans are shown in Fig. S3. Figure 2i shows a low-magnification HAADF-STEM image with a field of view of about 800 nm of the film with a 10 nm BTO capped sample. The BTO surface exhibits a rougher morphology, consistent with its polycrystalline nature. Figure 2j presents an atomic resolution STEM analysis of the local microstructure of the HZO. The semi-coherent interface between the HZO film and the LSMO bottom electrode, resulting from the domain-matching epitaxy growth mechanism [40], is clearly visible. The interface appears relatively sharp, which is attributed to its chemical reconstruction resulting in its La-rich composition [70]. The HZO layer is predominantly composed of orthorhombic grains, oriented along the [111]-type out-of-plane direction in agreement

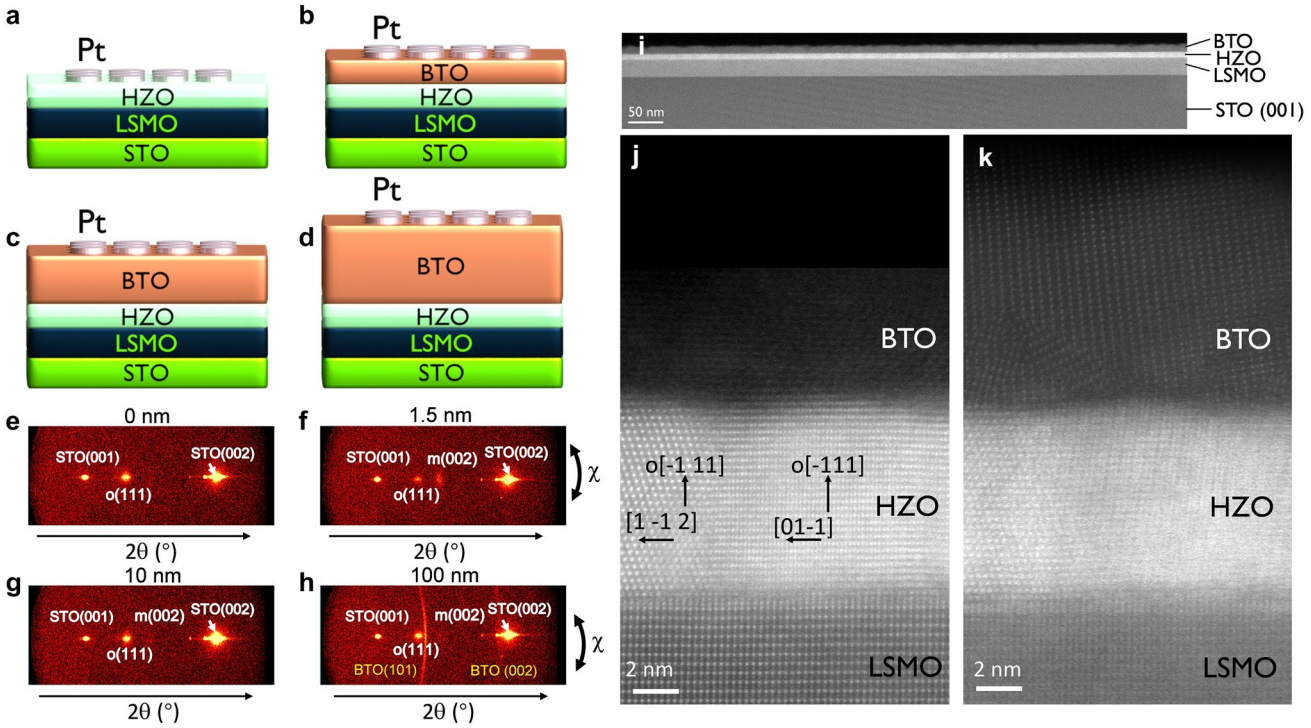

Fig. 2 **a-d** Schematic representation of the representative HZO/BTO samples with BTO thickness of 0, 1.5, 10, and 100 nm, respectively. **e–h** XRD 2θ–χ maps of HZO/BTO samples with BTO thickness of 0, 1.5, 10, and 100 nm, respectively. **i** Low magnification cross sectional HAADF-STEM image corresponding to the sample with a 10-nm-thick BTO layer. **j, k** Atomic resolution HAADF images of representative regions for the same sample. In image **k** the focus was optimized to maximize the contrast of the lattice fringes in crystalline BTO grains, to the detriment of the LSMO-HZO interface

https://doi.org/10.1007/s40820-026-02090-2

with XRD characterization. In this case, the BTO appears out of focus due to slight differences in ion milling rate and amorphization layer during lamella preparation. On the other hand, in Fig. 2k BTO grains appear in focus, and are coincidentally close to the tetragonal [110] zone axis, which allows the crystallinity of BTO to be more clearly inferred. Semicoherent growth of BTO on HZO is evident from the lattice alignment at the interface. The polycrystalline nature of BTO is better inferred in the wider image shown in Fig. S4.

Polarization–Voltage (P–V) loops measured at saturation voltage for the whole set of samples show P_r values between 7 and 15 μC cm^{-2} and a correlation between P_r and the intensity of the o(111) diffraction peak normalized to the m(002), as shown in Fig. 3a, b, respectively. In Fig. S5, we show ferroelectric characterization of a 100 nm BTO film on LSMO/STO, nominally grown under the same conditions as BTO capping. It can be observed that as anticipated the coercive electric field is much smaller than for HZO layer (of 225 kV cm^{-1}), along with sizeable (16 μC cm^{-2}) and robust against cycling ferroelectric polarization and leakage current slightly larger than that shown for most of the HZO capped samples (0.4 μA cm^{-2} at 1 V). Intensities of the diffraction peaks are extracted from Fig. S2. Therefore, it can be concluded that P_r is dominated by the different stabilization of o(111) phase depending on BTO thickness. The presence of depolarization electric field generated by BTO [71] is not evident. Among the films capped with BTO, the largest P_r value (15 μC cm^{-2}) is observed for the 10 nm BTO capped sample. Compared with other HfO_2- or ZrO_2-based systems that exhibit an optoelectric response [31–35], this value is clearly higher, as summarized in Fig. 3c and Table 1. Leakage curves shown in Fig. 3d display that leakage current does not significantly depend on thickness. It can be noted that the 1.5 and 10 nm BTO-capped samples exhibit slightly higher leakage, probably due to a larger number of defects arising from sample-to-sample variability. In fact, as mentioned, for BTO-capped films above 1.5 nm the leakage current at 1 V is smaller than 10^{-6} A cm^{-2}, lower than those previously reported for uncapped HZO films of similar thickness [72] and close to the very low values obtained in epitaxial La-doped HZO films [73].

3.2 Stable and Robust Ferroelectric Response

P–V measurements were taken at 4 V to better test the response upon cycling. At this voltage, sizeable switchable polarization is observed, even though full saturation polarization is not reached, which helps prevent breakdown. P–V loops of the single HZO layer and the samples with BTO capping of thicknesses 1.5, 10, and 100 nm are shown in Fig. 3e-h, respectively. P–V loops show that the P_r is 17.5 μC cm^{-2} for the non-capped sample, and it decreases to around 7.5 μC cm^{-2} for the 1.5 and 10 nm BTO-capped samples and to 2 μC cm^{-2} for the 100 nm-BTO capped sample. Clear ferroelectric switching peaks can be seen in I-V curves of the 0, 1.5, and 10 nm BTO capped samples, but less evident for the 100 nm one, as shown in Fig. S6. The reduction in polarization in BTO capped samples can be ascribed to the partial screening of the ferroelectric polarization of HZO, resulting from electron doping caused by the straddling band alignment at the HZO/BTO interface (Fig. 1d). Additionally, as shown in Fig. 3b, the orthorhombic phase fraction might also importantly influence P_r. It should also be noted that the bare HZO films exhibit a polarization lower than theoretical predictions, which estimate values in the range of 52–55 μC cm^{-2} [74, 75]. Experimentally, this corresponds to approximately 32 μC cm^{-2} for a (111)-oriented, phase-pure orthorhombic HfO_2 film, as reported elsewhere [76–79] indicating that orthorhombic phase fraction is around 50%-60% in the characterized films. In Fig. 3e-h, P–V curves after 10^6 cycles at 4 V are also shown. It can be observed that a similar response is observed among samples. Polarization variation upon cycling is small, disregarding the presence of any wake-up effect or significant fatigue. The loops were also recorded under illumination (see I-V curves in Fig. S6). The inset of Fig. 3a shows a picture of the used light spot. In brief, it can be observed that polarization, even after cycling, does not suffer significant variation under illumination, in agreement with the mentioned wide HfO_2's bandgap (≈ 6.0 eV) [29, 30].

In Fig. 4a, the full endurance measurements are shown, and the corresponding raw data for all samples are shown in Fig. S7. Figure 4a, shows that the polarization is sizeable and stable upon large number of cycles (10^8), except for 100 nm BTO that shows small P_r at the used cycling voltage and ferroelectric switching peaks can only be observed up to 10^7 cycles (Fig. S7). Figure 4a also shows the endurance data collected under illumination. The values are very similar to those obtained in the dark, further confirming the robustness of the ferroelectric character of the characterized samples. The absence of light effect on the ferroelectric endurance reveals, in addition to the robust ferroelectric response, the

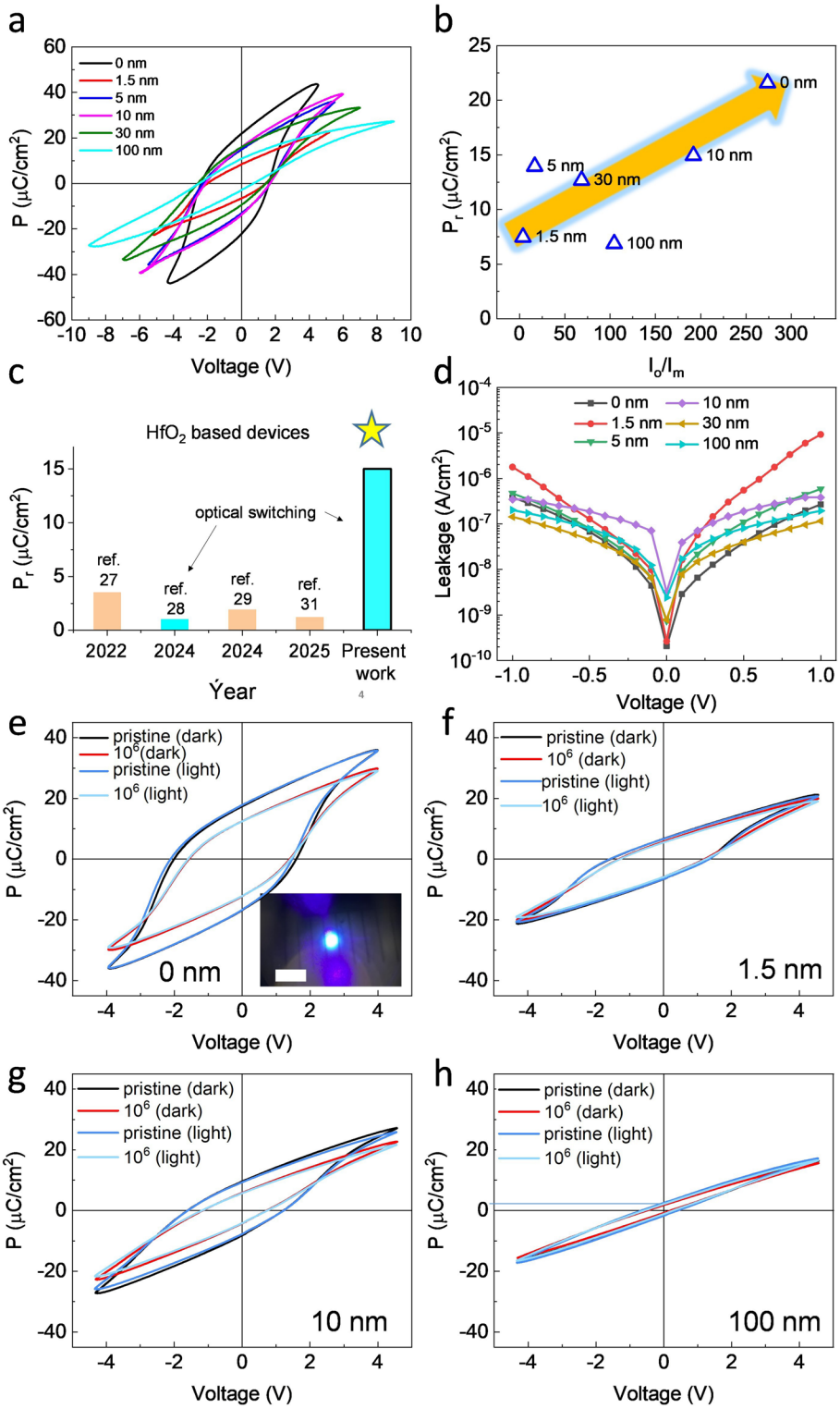

Fig. 3 **a** P–V loops of samples with BTO thickness of 0, 1.5, 5, 10, 30, and 100 nm. **b** Dependence of P_r on the ratio of peak intensities of o(111) and m(002) reflections, extracted from Fig. S2. **c** Summary of P_r values extracted from the literature and the present work in systems based on HfO_2 or ZrO_2 showing optoelectric response to visible light. **d** Leakage current of samples with BTO thickness of 0, 1.5, 5, 10, 30, and 100 nm. **e–h** P–V loops of HZO/BTO representative samples with BTO thickness of 0, 1.5, 10, and 100 nm, respectively, with and without illumination and in the pristine state and after 10^6 cycles

https://doi.org/10.1007/s40820-026-02090-2

absence of heating effects, as far as endurance in hafnia is highly sensitive to temperature [80]. Switching spectroscopy data are shown in Fig. 4b. It can be observed that the τ_w onset is near 50 ns, limited by the set-up time-constant. For increasing τ_w, P_r increases without full saturation, due to the presence of non-ferroelectric contributions at large τ_w [56]. τ_w-dependence under illumination also shows similar results, with variations inside the junction to junction variance. Raw data for switching spectroscopy are shown in Fig. S8.

3.3 Optical Switching of Polarization

All in all, the results presented up to here indicate that the presence of BTO layer causes a decrease of P_r, while a good endurance and fast switching are observed, both robust under illumination. Figure 5a-c shows PFM phase maps for the 1.5, 10, and 100 nm-thick samples collected on the BTO surface (without Pt), respectively, obtained after applying -8 V in the darker region and + 8 V in the brighter inner region. There is 180° phase contrast in all cases, indicating that polarization is pointing upwards in the dark region and downwards in the bright region, as indicated. Outer region corresponds to the as-grown state, which shows similar contrast to that obtained after + 8 V, and thus the as-grown samples present a downwards state. Figure 5d-f corresponds to PFM phase maps collected in the same region after illumination. It can be observed that for the 1.5 nm-BTO sample the contrast almost remains. Only some bright spots can be observed in the initially upwards region. This is not the case for 10 and 100 nm capped samples, where absence of 180° phase contrast is observed, indicating that in the dark regions of Fig. 5b, c, the polarization has switched from upwards to downwards. This indicates that the optical switching of polarization occurs more efficiently for thicker BTO layer. This agrees with the expected larger photogenerated charges due to larger light absorption, if the BTO-capping layer is thicker, which results in large E_{PV} (Fig. 1) and thus a more efficient optical switching of polarization. Indeed, Fig. S9 shows that polarization is not switched even after 10 min of illumination in same conditions for a non-capped sample. The residual contrast after illumination is because extrinsic charging effects can remain. Corresponding PFM amplitude images of Fig. 5 are shown in Fig. S10. PFM phase images collected after various illumination times are shown in Fig. S11 and allow to conclude that for 30 s illumination most of the ferroelectric domains that were pointing upwards have switched downwards. Instead for 1 s the polarization switching is partial, indicating that using the given conditions switching time is around or near above 1 s, which is comparable to switching time reported in other systems based on hafnia [32] as summarized in Table 1. Figure S12, where equivalent experiments are shown for 2 and 4 nm HZO layers with 10 nm BTO on top, shows that HZO layer thickness do not significantly impact on the observed optical polarization switching as expected by the fact that ferroelectricity in epitaxial HZO is preserved down to the ultrathin limit [81, 82]. Note that for the ferroelectric characterization shown in Figs. 3 and 4, the Pt top electrode is present and the device is connected to the electrical measurement system. As a result, photogenerated carriers in the BTO layer do not accumulate at the interface but instead flow through the circuit (Fig. 5g). Consequently,

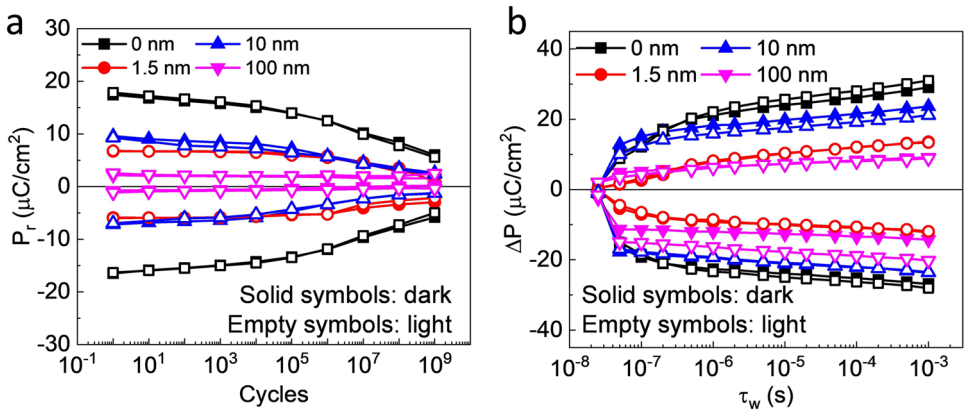

Fig. 4 **a** Endurance measured at 1 MHz and 4.5 V cycling voltage for 1.5, 10, and 100 nm samples and at 1 MHz and 4 V for the bare HZO film in the dark (solid symbols) and with illumination (open symbols). **b** Switching spectroscopy plots at 4.5, 5, 6, and 9 V writing and reading amplitudes for 0, 1.5, 10, and 100 nm samples, respectively, in the dark (solid symbols) and with illumination (open symbols)

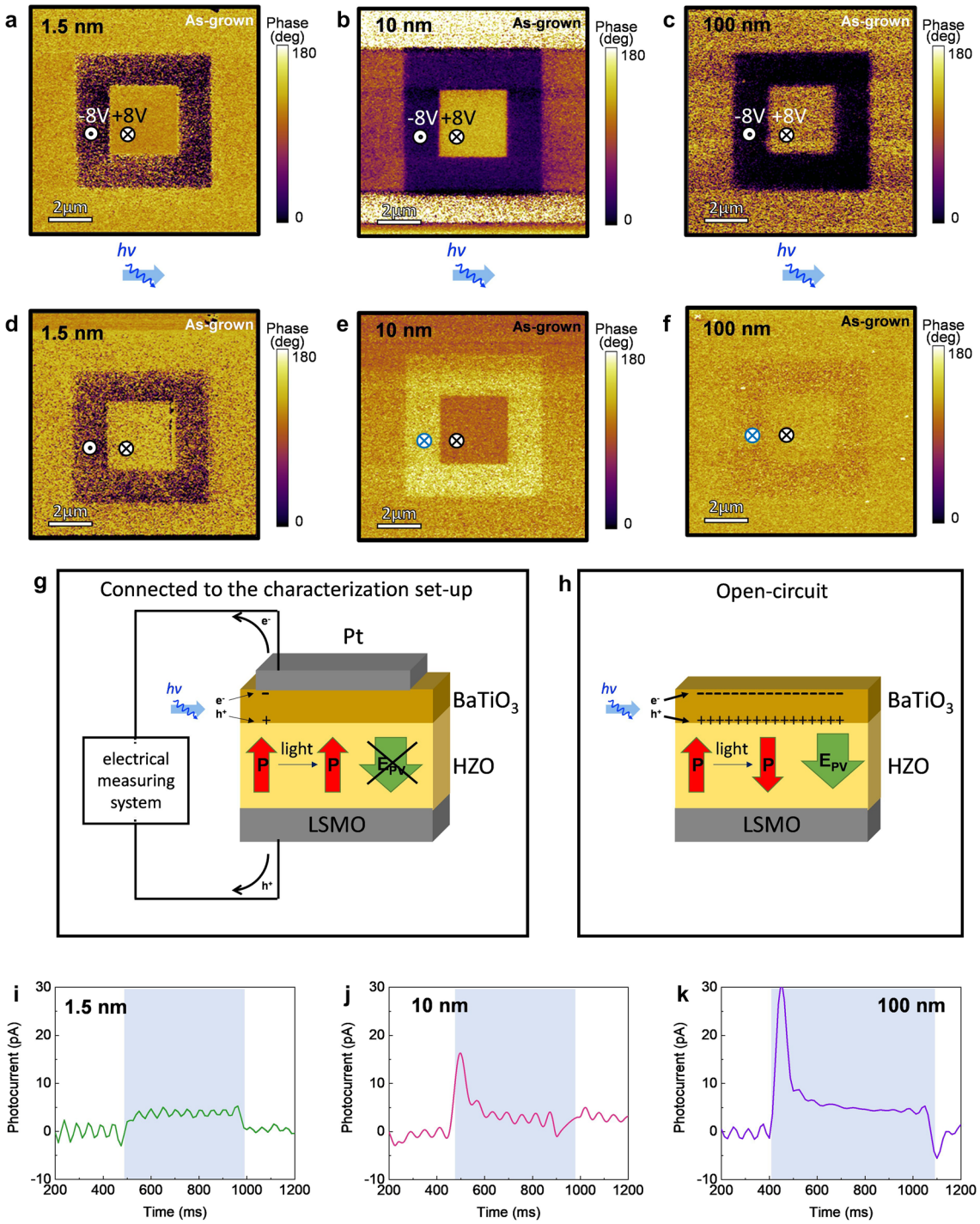

Fig. 5 PFM phase images after **a-c** electrical poling and waiting for 60 s in the dark and **d-f** after illuminating during 60 s for 1.5, 10, and 100 nm samples, respectively. Arrows indicate the polarization state and voltage the electrical writing voltage. In (**d-f**) blue arrows indicate optical polarization switching. **g, h** Sketch of the different charge flow behavior of the system while performing macroscopic ferroelectric characterization using Pt top electrodes connected to the measuring set-up and while performing PFM characterization without Pt top electrodes in open-circuit conditions, respectively. **i-k** I_{SC} dependence on time for 1.5, 10, and 100 nm samples, respectively. Bluish background indicates the timeframe when the sample was illuminated

https://doi.org/10.1007/s40820-026-02090-2

E_{PV} is not generated. In contrast, during PFM characterization the sample is in open-circuit conditions, so charges can only recombine or accumulate at the interfaces. This leads to the generation of E_{PV}, which drives the optically induced polarization switching (Fig. 5h), as anticipated in the description of Fig. 1b. Indeed, Fig. 5i-k shows the short-circuit photocurrent (I_{SC}) response measured using Pt top electrodes for the 1.5, 10, and 100 nm HZO/BTO samples, respectively. It can be observed that although the response is small, it is sizeable. As expected, I_{SC} increases with BTO thickness, consistent with the higher absorption of thicker films as described by Beer-Lambert's law and with the absence of optical switching for the 1.5 nm BTO sample. It can be also observed that the current is positive indicating that the electric field is directed downwards (as depicted in Figs. 1b and 5h) thus dictating the final state after illumination as downwards. The current peaks, at the moment of illumination start–end, if present, correspond to charging and discharging processes. No significant modulation of the I_{SC} with the preset polarization state is observed. A similar absence of I_{SC} dependence on polarization has been previously reported in systems based on different ferroelectric materials [53, 83–85], highlighting the predominant role of internal (built-in) electric fields over those associated with ferroelectric polarization. Indeed, the final polarization state is consistently oriented downwards irrespectively of the initial polarization sign, and the modification of the final state would only be possible through modification of the internal electric fields, as reported elsewhere [28]. In summary, we have demonstrated that the BTO capping layer plays a key role due to its high polarizability and its efficiency as a light absorber. Doped $BiFeO_3$ constitutes an interesting alternative, as it combines a comparatively reduced bandgap (≈2.7 eV) with a large remanent polarization in the range of 60–100 μC cm^{-2} [86–89]. In contrast, $Pb_xZr_{1-x}TiO_3$, another archetypal ferroelectric, is less suitable due to its larger bandgap (> 3.5 eV) [90, 91]. It should be noted, however, that both material families contain Bi and Pb, which are considered toxic and therefore limit their prospects for technological applications, despite their relevance for fundamental studies. Hexagonal manganites, such as $YMnO_3$ and $LuMnO_3$ [83, 92, 93], represent another interesting alternative, as they exhibit very narrow bandgaps (≈1.5 eV). Nevertheless, their relatively low polarization (≈5 μC cm^{-2}), substantially smaller than that of HZO, may be detrimental to the overall ferroelectric response. Exploring the broad materials family of two-dimensional ferroelectrics is also a promising research direction, as these systems can display a wide range of bandgaps, although they typically also exhibit low remanent polarization values [94, 95]. Non ferroelectric materials such as TiO_2, which exhibits a bandgap at the edge of the visible spectrum (E_g = 3.05 eV [96]) and a high permittivity (ranging from 30 to 120 depending on the stabilized phase [97, 98]), can also be considered promising candidates for similar applications.

4 Conclusions

We have shown that the HZO/BTO system presents robust ferroelectric properties with fast switching response, being the BTO thickness of 10 nm optimal. The crystalline quality of both HZO and BTO layers account for the observed good ferroelectric properties, i.e., P_r = 15 μC cm^{-2}, leakage current under 10^{-6} A cm^{-2} at 1 V, endurance up to 10^8 cycles and measured response time as fast as 50 ns (limited by the set-up). This performance exceeds that of previously reported HfO_2- and ZrO_2-based systems exhibiting optoelectric responses (Table 1). The sizeable photoresponse allows the optical switching of the polarization, as confirmed by PFM. In the studied system, BTO is responsible for the light absorption and photocarrier generation. Our findings establish a clear pathway for the development of high-performance photoferroelectric memory devices based on ferroelectric HfO_2.

Acknowledgements Financial support from the Spanish Ministry of Science, Innovation and Universities (MCIN/AEI/https://doi.org/10.13039/501100011033), through the Severo Ochoa MATRANS42 (CEX2023-001263-S) and CEX2023-001286-S, PDC2023-145874-I00, PID2023-147211OB-C21, PID2023-147211OB-C22 and TED2021-130453B-C21 projects, from Generalitat de Catalunya (2021 SGR 00804) and from Gobierno de Aragon project E13_23R is acknowledged. W.D. is financially supported by China Scholarship Council (CSC) with No. 202208310089. W.D. work has been done as a part of her Ph.D. program in Materials Science at Universitat Autònoma de Barcelona. We acknowledge the assistance of the ICMAB-CSIC Scientific & Technical Services: Thin Films Laboratory (Raul Solanas and Victor Pardo) and X-ray Diffraction Laboratory (Anna Crespi, Joan Esquius and Francisco Javier Campos). Authors acknowledge the use of instrumentation as well as the technical advice provided by the National Facility ELECMI ICTS, node «Laboratorio de Microscopias Avanzadas (LMA)» at «Universidad de Zaragoza».

Author Contributions Wenjing Dong, Huan Tan, Jingye Zou, Alberto Quintana, Tingfeng Song, César Magén, Claudio Cazorla contributed to conceptualization, data curation, formal analysis, investigation, methodology, writing-review and editing. Ignasi Fina and Florencio Sánchez contributed to conceptualization, funding

acquisition, data curation, supervision, and writing-original draft and editing.

Declarations

Conflict of interest The authors declare no conflict of interest. They have no known competing financial interests or personal relationships that could have influenced the work reported in this paper.

Supplementary Information The online version contains supplementary material available at https://doi.org/10.1007/s40820-026-02090-2.

References

1. O. Auciello, J.F. Scott, R. Ramesh, The physics of ferroelectric memories. Phys. Today **51**(7), 22–27 (1998). https://doi.org/10.1063/1.882324
2. T. Mikolajick, S. Slesazeck, M.H. Park, U. Schroeder, Ferroelectric hafnium oxide for ferroelectric random-access memories and ferroelectric field-effect transistors. MRS Bull. **43**(5), 340–346 (2018). https://doi.org/10.1557/mrs.2018.92
3. M.H. Park, Y.H. Lee, T. Mikolajick, U. Schroeder, C.S. Hwang, Review and perspective on ferroelectric HfO_2-based thin films for memory applications. MRS Commun. **8**(3), 795–808 (2018). https://doi.org/10.1557/mrc.2018.175
4. M.H. Park, D. Kwon, U. Schroeder, T. Mikolajick, Binary ferroelectric oxides for future computing paradigms. MRS Bull. **46**(11), 1071–1079 (2021). https://doi.org/10.1557/s43577-021-00210-4
5. Y. Sun, H. Li, F. Yu, J. Zhao, Y. Li et al., 1T1C 3D HZO FeRAM with high retention (>125 °C) and high endurance (>1E13) for embedded nonvolatile memory application, in *2025 Symposium on VLSI Technology and Circuits (VLSI Technology and Circuits)., IEEE* (2025). pp. 1–3 https://doi.org/10.23919/vlsitechnologyandcir65189.2025.11074853
6. N. Ramaswamy, A. Calderoni, J. Zahurak, G. Servalli, A. Chavan et al., NVDRAM: a 32Gb dual layer 3D stacked nonvolatile ferroelectric memory with near-DRAM performance for demanding AI workloads, in *2023 International Electron Devices Meeting (IEDM)*. San Francisco. IEEE, (2023). pp. 1–4. https://doi.org/10.1109/iedm45741.2023.10413848
7. Y. Sun, H. Wang, D. Xie, Recent advance in synaptic plasticity modulation techniques for neuromorphic applications. Nano-Micro Lett. **16**(1), 211 (2024). https://doi.org/10.1007/s40820-024-01445-x
8. T. Schenk, M. Pešić, S. Slesazeck, U. Schroeder, T. Mikolajick, Memory technology: a primer for material scientists. Rep. Prog. Phys. **83**(8), 086501 (2020). https://doi.org/10.1088/1361-6633/ab8f86
9. S. Manipatruni, D.E. Nikonov, C.-C. Lin, T.A. Gosavi, H. Liu et al., Scalable energy-efficient magnetoelectric spin-orbit logic. Nature **565**(7737), 35–42 (2019). https://doi.org/10.1038/s41586-018-0770-2
10. R. Guo, L. You, Y. Zhou, Z.S. Lim, X. Zou et al., Non-volatile memory based on the ferroelectric photovoltaic effect. Nat. Commun. **4**, 1990 (2013). https://doi.org/10.1038/ncomms2990
11. B. Kundys, M. Viret, D. Colson, D.O. Kundys, Light-induced size changes in $BiFeO_3$ crystals. Nat. Mater. **9**(10), 803–805 (2010). https://doi.org/10.1038/nmat2807
12. S.Y. Yang, J. Seidel, S.J. Byrnes, P. Shafer, C.-H. Yang et al., Above-bandgap voltages from ferroelectric photovoltaic devices. Nat. Nanotechnol. **5**(2), 143–147 (2010). https://doi.org/10.1038/nnano.2009.451
13. V. Iurchuk, D. Schick, J. Bran, D. Colson, A. Forget et al., Optical writing of magnetic properties by remanent photostriction. Phys. Rev. Lett. **117**(10), 107403 (2016). https://doi.org/10.1103/PhysRevLett.117.107403
14. X. Zhang, X. Guo, B. Cui, J. Yun, J. Mao et al., Light modulation of magnetization switching in PMN-PT/Ni heterostructure. Appl. Phys. Lett. **116**(13), 132405 (2020). https://doi.org/10.1063/1.5145284
15. D.A. Ochoa, E. Menéndez, J. López-Sánchez, A. Del Campo, Z. Ma et al., Reversible optical control of magnetism in engineered artificial multiferroics. Nanoscale **16**(9), 4900–4908 (2024). https://doi.org/10.1039/d3nr05520e
16. M.A. Iqbal, H. Xie, L. Qi, W.-C. Jiang, Y.-J. Zeng, Recent advances in ferroelectric-enhanced low-dimensional optoelectronic devices. Small **19**(16), e2205347 (2023). https://doi.org/10.1002/smll.202205347
17. Y. Wen, Y. Cao, H. Ren, X. Du, J. Guo et al., Ferroelectric optical memristors enabled by non-volatile electro-optic effect. Adv. Mater. **37**(8), e2417658 (2025). https://doi.org/10.1002/adma.202417658
18. J.H. Wei, Z. Wang, W. Yu, T. Wu, Optically controlled electroresistance and electrically controlled photovoltage in ferroelectric tunnel junctions. Nat. Commun. **7**, 10808 (2016). https://doi.org/10.1038/ncomms10808
19. F. Rubio-Marcos, A. Del Campo, P. Marchet, J.F. Fernández, Ferroelectric domain wall motion induced by polarized light. Nat. Commun. **6**, 6594 (2015). https://doi.org/10.1038/ncomms7594
20. F. Rubio-Marcos, D.A. Ochoa, A. Del Campo, M.A. García, G.R. Castro et al., Reversible optical control of macroscopic

polarization in ferroelectrics. Nat. Photonics **12**(1), 29–32 (2018). https://doi.org/10.1038/s41566-017-0068-1

21. H. Akamatsu, Y. Yuan, V.A. Stoica, G. Stone, T. Yang et al., Light-activated gigahertz ferroelectric domain dynamics. Phys. Rev. Lett. **120**(9), 096101 (2018). https://doi.org/10.1103/PhysRevLett.120.096101
22. M.-M. Yang, M. Alexe, Light-induced reversible control of ferroelectric polarization in $BiFeO_3$. Adv. Mater. **30**(14), e1704908 (2018). https://doi.org/10.1002/adma.201704908
23. Z.-D. Luo, D.-S. Park, M.-M. Yang, M. Alexe, Light-controlled nanoscopic writing of electronic memories using the tip-enhanced bulk photovoltaic effect. ACS Appl. Mater. Interfaces **11**(8), 8276–8283 (2019). https://doi.org/10.1021/acsami.8b22638
24. A. Lipatov, P. Sharma, A. Gruverman, A. Sinitskii, Optoelectrical molybdenum disulfide (MoS_2): ferroelectric memories. ACS Nano **9**(8), 8089–8098 (2015). https://doi.org/10.1021/acsnano.5b02078
25. Z.-D. Luo, X. Xia, M.-M. Yang, N.R. Wilson, A. Gruverman et al., Artificial optoelectronic synapses based on ferroelectric field-effect enabled 2D transition metal dichalcogenide memristive transistors. ACS Nano **14**(1), 746–754 (2020). https://doi.org/10.1021/acsnano.9b07687
26. X. Long, H. Tan, F. Sánchez, I. Fina, J. Fontcuberta, Nonvolatile optical switch of resistance in photoferroelectric tunnel junctions. Nat. Commun. **12**(1), 382 (2021). https://doi.org/10.1038/s41467-020-20660-9
27. X. Long, H. Tan, F. Sánchez, I. Fina, J. Fontcuberta, Disentangling electronic and thermal contributions to light-induced resistance switching in $BaTiO_3$ ferroelectric tunnel junction. J. Appl. Phys. **132**(21), 214103 (2022). https://doi.org/10.1063/5.0125040
28. H. Tan, G. Castro, J. Lyu, P. Loza-Alvarez, F. Sánchez et al., Control of up-to-down/down-to-up light-induced ferroelectric polarization reversal. Mater. Horiz. **9**(9), 2345–2352 (2022). https://doi.org/10.1039/d2mh00644h
29. Y.H. Wong, K.Y. Cheong, Band alignment and enhanced breakdown field of simultaneously oxidized and nitrided Zr film on Si. Nanoscale Res. Lett. **6**(1), 489 (2011). https://doi.org/10.1186/1556-276X-6-489
30. N.V. Nguyen, A.V. Davydov, D. Chandler-Horowitz, M.M. Frank, Sub-bandgap defect states in polycrystalline hafnium oxide and their suppression by admixture of silicon. Appl. Phys. Lett. **87**(19), 192903 (2005). https://doi.org/10.1063/1.2126136
31. M. Kumar, H. Seo, High-performing self-powered photosensing and reconfigurable pyro-photoelectric memory with ferroelectric hafnium oxide. Adv. Mater. **34**(5), 2270041 (2022). https://doi.org/10.1002/adma.202270041
32. H. Tan, A. Quintana, N. Dix, S. Estandía, J. Sort et al., Photovoltaic-driven dual optical writing and non-destructive voltage-less reading of polarization in ferroelectric $Hf_{0.5}Zr_{0.5}O_2$ for energy efficient memory devices. Nano Energy **123**, 109384 (2024). https://doi.org/10.1016/j.nanoen.2024.109384
33. A. Imran, X. He, H. Tabassum, Q. Zhu, G. Dastgeer et al., Neuromorphic vision sensor driven by ferroelectric HfAlO. Materials Today Nano **26**, 100473 (2024). https://doi.org/10.1016/j.mtnano.2024.100473
34. R. Eskandari, X. Zhang, L.M. Malkinski, Polarization-dependent photovoltaic effect in ferroelectric-semiconductor system. Appl. Phys. Lett. **110**(12), 121105 (2017). https://doi.org/10.1063/1.4978749
35. N.E. Silva, A.R. Jayakrishnan, A. Kaim, K. Gwozdz, L. Domingues et al., Ultra-sensitive, self-powered, CMOS-compatible near-infrared photodetectors for wide-ranging applications. Adv. Funct. Mater. **35**(14), 2416979 (2025). https://doi.org/10.1002/adfm.202416979
36. J. Lyu, I. Fina, R. Solanas, J. Fontcuberta, F. Sánchez, Robust ferroelectricity in epitaxial $Hf_{1/2}Zr_{1/2}O_2$ thin films. Appl. Phys. Lett. **113**(8), 082902 (2018). https://doi.org/10.1063/1.5041715
37. Y. Wei, P. Nukala, M. Salverda, S. Matzen, H.J. Zhao et al., A rhombohedral ferroelectric phase in epitaxially strained $Hf_{0.5}Zr_{0.5}O_2$ thin films. Nat. Mater. **17**(12), 1095–1100 (2018). https://doi.org/10.1038/s41563-018-0196-0
38. J. Lyu, I. Fina, F. Sánchez, Fatigue and retention in the growth window of ferroelectric $Hf_{0.5}Zr_{0.5}O_2$ thin films. Appl. Phys. Lett. **117**(7), 072901 (2020). https://doi.org/10.1063/5.0017738
39. I. Fina, F. Sánchez, Epitaxial ferroelectric HfO_2 films: growth, properties, and devices. ACS Appl. Electron. Mater. **3**(4), 1530–1549 (2021). https://doi.org/10.1021/acsaelm.1c00110
40. S. Estandía, N. Dix, M.F. Chisholm, I. Fina, F. Sánchez, Domain-matching epitaxy of ferroelectric $Hf_{0.5}Zr_{0.5}O_2(111)$ on $La_{2/3}Sr_{1/3}MnO_3(001)$. Cryst. Growth Des. **20**(6), 3801–3806 (2020). https://doi.org/10.1021/acs.cgd.0c00095
41. S. Estandía, J. Gàzquez, M. Varela, N. Dix, M. Qian et al., Critical effect of the bottom electrode on the ferroelectricity of epitaxial $Hf_{0.5}Zr_{0.5}O_2$ thin films. J. Mater. Chem. C **9**(10), 3486–3492 (2021). https://doi.org/10.1039/d0tc05853j
42. J. Sun, L. Ding, Linearly polarization-sensitive perovskite photodetectors. Nano-Micro Lett. **15**(1), 90 (2023). https://doi.org/10.1007/s40820-023-01048-y
43. L. Zhang, L. Mei, K. Wang, Y. Lv, S. Zhang et al., Advances in the application of perovskite materials. Nano-Micro Lett. **15**(1), 177 (2023). https://doi.org/10.1007/s40820-023-01140-3
44. X. Li, S. Aftab, M. Mukhtar, F. Kabir, M.F. Khan et al., Exploring nanoscale perovskite materials for next-generation photodetectors: a comprehensive review and future directions. Nano-Micro Lett. **17**(1), 28 (2024). https://doi.org/10.1007/s40820-024-01501-6
45. J.Y. Chang, C.R. Chinjen, R.H. Tsou, C.Y. Huang, C.C. Sun et al., Photorefractive effect in hydrogen-reduced $BaTiO_3$. Opt. Commun. **138**(1–3), 101–104 (1997). https://doi.org/10.1016/S0030-4018(97)00036-9
46. W.L. Warren, D. Dimos, Photoinduced hysteresis changes and charge trapping in $BaTiO_3$ dielectrics. Appl. Phys. Lett. **64**(7), 866–868 (1994). https://doi.org/10.1063/1.110978

47. W.T.H. Koch, R. Munser, W. Ruppel, P. Würfel, Bulk photovoltaic effect in $BaTiO_3$. Solid State Commun. **17**(7), 847–850 (1975). https://doi.org/10.1016/0038-1098(75)90735-8
48. A.J. Garza, G.E. Scuseria, Predicting band gaps with hybrid density functionals. J. Phys. Chem. Lett. **7**(20), 4165–4170 (2016). https://doi.org/10.1021/acs.jpclett.6b01807
49. Z. Liu, C. Menéndez, J. Shenoy, J.N. Hart, C.C. Sorrell et al., Strain engineering of oxide thin films for photocatalytic applications. Nano Energy **72**, 104732 (2020). https://doi.org/10.1016/j.nanoen.2020.104732
50. Z. Liu, B. Wang, D. Chu, C. Cazorla, First-principles high-throughput screening of bulk piezo-photocatalytic materials for sunlight-driven hydrogen production. J. Mater. Chem. A **10**(35), 18132–18146 (2022). https://doi.org/10.1039/d2ta05941j
51. R. Rurali, C. Escorihuela-Sayalero, J.L. Tamarit, J. Íñiguez-González, C. Cazorla, Giant photocaloric effects across a vast temperature range in ferroelectric perovskites. Phys. Rev. Lett. **133**(11), 116401 (2024). https://doi.org/10.1103/PhysRevLett.133.116401
52. C. Cazorla, C. Escorihuela-Sayalero, J. Carrete, J. Íñiguez-González, R. Rurali, Optical control of the thermal conductivity in $BaTiO_3$. Adv. Funct. Mater. **35**(48), e2425424 (2025). https://doi.org/10.1002/adfm.202425424
53. F. Liu, I. Fina, D. Gutiérrez, G. Radaelli, R. Bertacco et al., Selecting steady and transient photocurrent response in $BaTiO_3$ films. Adv. Electron. Mater. **1**(9), 1500171 (2015). https://doi.org/10.1002/aelm.201500171
54. R. Meyer, R. Waser, K. Prume, T. Schmitz, S. Tiedke, Dynamic leakage current compensation in ferroelectric thin-film capacitor structures. Appl. Phys. Lett. **86**(14), 142907 (2005). https://doi.org/10.1063/1.1897425
55. I. Fina, L. Fàbrega, E. Langenberg, X. Martí, F. Sánchez et al., Nonferroelectric contributions to the hysteresis cycles in manganite thin films: a comparative study of measurement techniques. J. Appl. Phys. **109**(7), 074105 (2011). https://doi.org/10.1063/1.3555098
56. T. Song, F. Sánchez, I. Fina, Impact of non-ferroelectric phases on switching dynamics in epitaxial ferroelectric $Hf_{0.5}Zr_{0.5}O_2$ films. APL Mater. **10**(3), 031108 (2022). https://doi.org/10.1063/5.0083661
57. M.N. Polyanskiy, Refractive index database. 25/03/2022.
58. S.H. Wemple, Polarization fluctuations and the optical-absorption edge in $BaTiO_3$. Phys. Rev. B **2**(7), 2679–2689 (1970). https://doi.org/10.1103/physrevb.2.2679
59. M.L. Moreira, M.F.C. Gurgel, G.P. Mambrini, E.R. Leite, P.S. Pizani et al., Photoluminescence of barium titanate and barium zirconate in multilayer disordered thin films at room temperature. J. Phys. Chem. A **112**(38), 8938–8942 (2008). https://doi.org/10.1021/jp801610y
60. J.Y. Chang, M.H. Garrett, H.P. Jenssen, C. Warde, Intensity dependent absorption/transparency of a reducing $BaTiO_3$. Appl. Phys. Lett. **63**(26), 3598–3600 (1993). https://doi.org/10.1063/1.110108
61. T. Zhao, Z.-H. Chen, F. Chen, H.-B. Lu, G.-Z. Yang et al., Electrical and optical properties of strongly reduced epitaxial $BaTiO_{3-x}$ thin films. Appl. Phys. Lett. **77**(26), 4338–4340 (2000). https://doi.org/10.1063/1.1334353
62. V.V. Laguta, A.M. Slipenyuk, I.P. Bykov, M.D. Glinchuk, M. Maglione et al., Electron spin resonance investigation of oxygen-vacancy-related defects in $BaTiO_3$ thin films. Appl. Phys. Lett. **87**(2), 022903 (2005). https://doi.org/10.1063/1.1954900
63. M. Choi, F. Oba, I. Tanaka, Electronic and structural properties of the oxygen vacancy in $BaTiO_3$. Appl. Phys. Lett. **98**(17), 172901 (2011). https://doi.org/10.1063/1.3583460
64. B.J. Rodriguez, C. Callahan, S.V. Kalinin, R. Proksch, Dual-frequency resonance-tracking atomic force microscopy. Nanotechnology **18**(47), 475504 (2007). https://doi.org/10.1088/0957-4484/18/47/475504
65. H. Tan, J. Lyu, Y. Sheng, P. Machado, T. Song et al., A transversal approach to predict surface charge compensation in piezoelectric force microscopy. Appl. Surf. Sci. **607**, 154991 (2023). https://doi.org/10.1016/j.apsusc.2022.154991
66. C. Cazorla, J. Boronat, Simulation and understanding of atomic and molecular quantum crystals. Rev. Mod. Phys. **89**(3), 035003 (2017). https://doi.org/10.1103/revmodphys.89.035003
67. J.P. Perdew, A. Ruzsinszky, G.I. Csonka, O.A. Vydrov, G.E. Scuseria et al., Restoring the density-gradient expansion for exchange in solids and surfaces. Phys. Rev. Lett. **100**(13), 136406 (2008). https://doi.org/10.1103/PhysRevLett.100.136406
68. G. Kresse, J. Furthmüller, Efficient iterative schemes for ab initio total-energy calculations using a plane-wave basis set. Phys. Rev. B **54**(16), 11169–11186 (1996). https://doi.org/10.1103/physrevb.54.11169
69. P.E. Blöchl, Projector augmented-wave method. Phys. Rev. B **50**(24), 17953–17979 (1994). https://doi.org/10.1103/physrevb.50.17953
70. S. Estandía, T. Cao, R. Mishra, I. Fina, F. Sánchez et al., Insights into the atomic structure of the interface of ferroelectric $Hf_{0.5}Zr_{0.5}O_2$ grown epitaxially on $La_{2/3}Sr_{1/3}MnO_3$. Phys. Rev. Mater. **5**(7), 074410 (2021). https://doi.org/10.1103/physrevmaterials.5.074410
71. A.K. Tagantsev, G. Gerra, Interface-induced phenomena in polarization response of ferroelectric thin films. J. Appl. Phys. **100**(5), 051607 (2006). https://doi.org/10.1063/1.2337009
72. J. Lyu, I. Fina, R. Solanas, J. Fontcuberta, F. Sánchez, Growth window of ferroelectric epitaxial $Hf_{0.5}Zr_{0.5}O_2$ thin films. ACS Appl. Electron. Mater. **1**(2), 220–228 (2019). https://doi.org/10.1021/acsaelm.8b00065
73. T. Song, R. Bachelet, G. Saint-Girons, R. Solanas, I. Fina et al., Epitaxial ferroelectric La-doped $Hf_{0.5}Zr_{0.5}O_2$ thin films. ACS Appl. Electron. Mater. **2**(10), 3221–3232 (2020). https://doi.org/10.1021/acsaelm.0c00560

 https://doi.org/10.1007/s40820-026-02090-2

74. T.D. Huan, V. Sharma, G.A. Rossetti, R. Ramprasad, Pathways towards ferroelectricity in hafnia. Phys. Rev. B **90**(6), 064111 (2014). https://doi.org/10.1103/physrevb.90.064111
75. F. Delodovici, P. Barone, S. Picozzi, Trilinear-coupling-driven ferroelectricity in HfO_2. Phys. Rev. Mater. **5**(6), 064405 (2021). https://doi.org/10.1103/physrevmaterials.5.064405
76. S. Estandía, N. Dix, J. Gazquez, I. Fina, J. Lyu et al., Engineering ferroelectric $Hf_{0.5}Zr_{0.5}O_2$ thin films by epitaxial stress. ACS Appl. Electron. Mater. **1**(8), 1449–1457 (2019). https://doi.org/10.1021/acsaelm.9b00256
77. T. Song, H. Tan, A.-C. Robert, S. Estandia, J. Gázquez et al., Synergetic contributions of chemical doping and epitaxial stress to polarization in ferroelectric HfO_2 films. Appl. Mater. Today **29**, 101621 (2022). https://doi.org/10.1016/j.apmt.2022.101621
78. T. Song, H. Tan, S. Estandía, J. Gàzquez, M. Gich et al., Improved polarization and endurance in ferroelectric $Hf_{0.5}Zr_{0.5}O_2$ films on $SrTiO_3$(110). Nanoscale **14**(6), 2337–2343 (2022). https://doi.org/10.1039/D1NR06983G
79. T. Song, R. Solanas, M. Qian, I. Fina, F. Sánchez, Large enhancement of ferroelectric polarization in $Hf_{0.5}Zr_{0.5}O_2$ films by low plasma energy pulsed laser deposition. J. Mater. Chem. C **10**(3), 1084–1089 (2022). https://doi.org/10.1039/d1tc05387f
80. N. Liu, Y. Liu, H. Wu, J. Fang, W. Tang et al., Reliable high-temperature ferroelectric memories based on $Hf_{0.5}Zr_{0.5}O_2$ film. Ceram. Int. **51**(14), 19138–19144 (2025). https://doi.org/10.1016/j.ceramint.2025.02.092
81. M. Cervo Sulzbach, H. Tan, S. Estandía, J. Gàzquez, F. Sánchez et al., Polarization and resistive switching in epitaxial 2 nm $Hf_{0.5}Zr_{0.5}O_2$ tunnel junctions. ACS Appl. Electron. Mater. **3**(8), 3657–3666 (2021). https://doi.org/10.1021/acsaelm.1c00604
82. B. Prasad, V. Thakare, A. Kalitsov, Z. Zhang, B. Terris et al., Large tunnel electroresistance with ultrathin $Hf_{0.5}Zr_{0.5}O_2$ ferroelectric tunnel barriers. Adv. Electron. Mater. **7**(6), 2001074 (2021). https://doi.org/10.1002/aelm.202001074
83. Y. Sheng, I. Fina, M. Gospodinov, J. Fontcuberta, Switchable photovoltaic response in hexagonal $LuMnO_3$ single crystals. Appl. Phys. Lett. **118**(23), 232902 (2021). https://doi.org/10.1063/5.0053379
84. Y. Sheng, H. Tan, A. Quintana, M. Villa, J. Gázquez et al., Untwining polar contributions from light-polarization dependent photovoltaic response of $LuMnO_{3-}$ based ferroelectric capacitors. Acta Mater. **245**, 118601 (2023). https://doi.org/10.1016/j.actamat.2022.118601
85. P. Machado, P. Salles, A. Frebel, G. De Luca, E. Ros et al., Interface engineering in all-oxide photovoltaic devices based on photoferroelectric $BiFe_{0.9}Co_{0.1}O_3$ thin films. ACS Appl. Electron. Mater. **6**(11), 8251–8259 (2024). https://doi.org/10.1021/acsaelm.4c01533
86. T. Choi, S. Lee, Y.J. Choi, V. Kiryukhin, S.-W. Cheong, Switchable ferroelectric diode and photovoltaic effect in $BiFeO_3$. Science **324**(5923), 63–66 (2009). https://doi.org/10.1126/science.1168636
87. S.Y. Yang, L.W. Martin, S.J. Byrnes, T.E. Conry, S.R. Basu et al., Photovoltaic effects in $BiFeO_3$. Appl. Phys. Lett. **95**(6), 062909 (2009). https://doi.org/10.1063/1.3204695
88. G. Chen, J. Chen, W. Pei, Y. Lu, Q. Zhang et al., Bismuth ferrite materials for solar cells: current status and prospects. Mater. Res. Bull. **110**, 39–49 (2019). https://doi.org/10.1016/j.materresbull.2018.10.011
89. L. You, A. Abdelsamie, Y. Zhou, L. Chang, Z.S. Lim et al., Revisiting the ferroelectric photovoltaic properties of vertical $BiFeO_3$ capacitors: a comprehensive study. ACS Appl. Mater. Interfaces **15**(9), 12070–12077 (2023). https://doi.org/10.1021/acsami.2c23023
90. C.H. Peng, J.-F. Chang, S.B. Desu, Optical properties of PZT, PLZT, and PNZT thin films. MRS Online Proc. Libr. **243**(1), 21–26 (1991). https://doi.org/10.1557/PROC-243-21
91. Y.P. Jiang, X.G. Tang, Q.X. Liu, Q. Li, A.L. Ding, Optical properties of $Pb(Zr_{0.53}Ti_{0.47})O_3$ thin films on Pt-coated Si substrates measured by spectroscopic ellipsometry in the UV–vis–NIR region. Mater. Sci. Eng. B **137**(1–3), 304–309 (2007). https://doi.org/10.1016/j.mseb.2006.11.025
92. Y. Sheng, I. Fina, M. Gospodinov, A.M. Schankler, A.M. Rappe et al., Bulk photovoltaic effect in hexagonal $LuMnO_3$-single crystals. Phys. Rev. B **104**(18), 184116 (2021). https://doi.org/10.1103/physrevb.104.184116
93. K. Miura, L. Zhang, D. Kiriya, A. Ashida, T. Yoshimura et al., Origin of the photoinduced current of strongly correlated $YMnO_3$ferroelectric epitaxial films. Jpn. J. Appl. Phys. **56**(10S), 10PB08 (2017). https://doi.org/10.7567/jjap.56.10pb08
94. C. Wang, Y. Zhang, D. Zhang, Y. Sun, T. Zhang et al., 2D van der Waals sliding ferroelectrics toward novel electronic devices. Small **21**(8), e2408375 (2025). https://doi.org/10.1002/smll.202408375
95. C. Wang, L. You, D. Cobden, J. Wang, Towards two-dimensional van der Waals ferroelectrics. Nat. Mater. **22**(5), 542–552 (2023). https://doi.org/10.1038/s41563-022-01422-y
96. J. Robertson, Band offsets of wide-band-gap oxides and implications for future electronic devices. J. Vacuum Sci. Technol. B Microelectron. Nanometer Struct. Process. Measure. and Phenomena **18**(3), 1785–1791 (2000). https://doi.org/10.1116/1.591472
97. L.J. Berberich, M.E. Bell, The dielectric properties of the rutile form of TiO_2. J. Appl. Phys. **11**(10), 681–692 (1940). https://doi.org/10.1063/1.1712721
98. S.K. Kim, W.-D. Kim, K.-M. Kim, C.S. Hwang, J. Jeong, High dielectric constant TiO_2 thin films on a Ru electrode grown at 250 °C by atomic-layer deposition. Appl. Phys. Lett. **85**(18), 4112–4114 (2004). https://doi.org/10.1063/1.1812832